Journal of
Materials Chemistry A

PAPER

View Article Online
View Journal | View Issue

Check for updates

Cite this: *J. Mater. Chem. A*, 2026, **14**, 15218

Harnessing slow photons in 3D silica photonic crystals for efficient and catalyst-free removal of chromophoric organic pollutants

Tharishinny Raja Mogan,*[a] Ruo Qi Ho,[a] Veronica Pereira,[a] Carice Chong,[a] Siew Kheng Boong,[a] Eugene Yee Shuen Chua[a] and Hiang Kwee Lee*[ab]

Received 21st November 2025
Accepted 1st March 2026

DOI: 10.1039/d5ta09484d

rsc.li/materials-a

The widespread release of chromophoric organic pollutants from industrial and municipal sources poses a critical threat to aquatic ecosystems and human health. While adsorption-based treatments offer rapid contaminant removal, they suffer from limited capacity and secondary waste generation arising from the spent adsorbent. Photocatalytic degradation provides a cleaner alternative but often relies on catalysts with poor stability and slow kinetics. Herein, we introduce a metal-free, catalyst-free water purification approach using chemically inert SiO_2 inverse opal photonic crystals that integrate high-capacity adsorption with visible-light-driven pollutant degradation. The three-dimensional periodic structure facilitates rapid pollutant uptake through interconnected porosity, while photonic bandgap effects and slow photon generation dramatically enhance light confinement. This optical effect enables efficient photodegradation of pre-adsorbed chromophoric organic pollutants using only visible light. Among the tested platforms, SiO_2 IO-343 demonstrates superior performance, achieving >90% adsorption within 1 hour and 95% photodegradation upon extended irradiation. Notably, its apparent reaction rate exceeds those of state-of-the-art semiconductor and hybrid photocatalysts by up to 17-fold, even though it lacks optically active or redox-functional components. Our findings position photonic crystal architectures as a promising class of robust, regenerable, and energy-efficient materials for advanced water treatment, notably offering a catalyst-free alternative for sustainable water purification.

1. Introduction

Water pollution continues to pose one of the most pressing global environmental threats, with profound implications for ecological stability, public health, and clean water accessibility.[1] A significant fraction of this pollution originates from anthropogenic organic contaminants released through industrial effluents, agricultural runoff, and municipal wastewater.[2,3] Among these, organic molecules that frequently contain aromatic frameworks and extended π-conjugated systems have drawn increasing attention due to their persistence, prevalence, and environmental impact.[4,5] Notably, these molecular structural features usually confer chromophoric properties, characterized by strong optical absorption across the visible spectrum. For instance, azo dyes and aromatic amines are common structural motifs in such compounds and are associated with genotoxicity, carcinogenicity, and endocrine disruption.[6,7] Given their persistence and harmful effects, effective strategies for eliminating these pollutants from aquatic environments are urgently needed to safeguard ecological integrity and human health.

Common water treatment technologies based on molecular adsorption remain among the most widely adopted approaches for the rapid removal (typically <1 h) of organic pollutants from aqueous environments.[8,9] Their operational simplicity, low energy requirements, and effectiveness in concentrating trace contaminants make them highly attractive for both large-scale treatment facilities and point-of-use systems. Materials such as activated carbon, zeolites, metal–organic frameworks (MOFs), and mesoporous silica have been extensively explored for this purpose due to their high surface area and tunable surface chemistry.[10–12] However, conventional adsorbents face several critical limitations that hinder their long-term applicability and environmental sustainability. Many require thermal activation, pH adjustment, or chemical additives to achieve optimal adsorption performance, which increases process complexity and operational costs.[13,14] More importantly, adsorption is inherently a finite process. Once the adsorbent becomes saturated, it forms a pollutant-laden material that represents a highly toxic and concentrated form of secondary waste, which must either be regenerated or safely discarded.

---

[a] *Division of Chemistry and Biological Chemistry, School of Chemistry, Chemical Engineering and Biotechnology, Nanyang Technological University, Singapore 637371, 21 Nanyang Link, Singapore. E-mail: hiangkwee@ntu.edu.sg; tharishinny.rm@ntu.edu.sg*

[b] *Institute of Materials Research and Engineering, The Agency for Science, Technology and Research (A*STAR), 2 Fusionopolis Way, #08-03, Innovis, 138634, Singapore*

Improper disposal risks the leaching of concentrated toxic compounds back into the environment, while regeneration often requires harsh solvents, elevated temperatures, or oxidizing agents that are energy-intensive and may compromise both the structural and chemical integrity of the adsorbent.[15,16]

Reaction-based decontamination strategies offer a compelling alternative to adsorption by actively transforming hazardous organic pollutants into less harmful or benign chemical species. Light-driven processes are particularly attractive for environmental remediation because they harness sunlight as a clean, abundant, and renewable energy source. These reactions can proceed either through direct photochemical interactions with pollutant molecules in which the chromophoric compounds undergo self-degradation upon irradiation (*e.g.*, photobleaching), or through the use of photocatalysts that absorb light and generate energetic electron–hole pairs.[17–19] These photogenerated charge carriers can subsequently initiate the formation of reactive chemical intermediates capable of mineralizing organic contaminants. Despite these advantages, reaction-based approaches remain relatively sluggish in pollutant removal when compared to the rapid efficiency of adsorption-based methods. Current systems often require several hours to achieve meaningful degradation, limiting their practicality for real-time or flow-through water treatment scenarios where immediate decontamination is essential.[20] Moreover, when photocarriers are not fully consumed by target reactants (*e.g.*, pollutant molecules), they can accumulate within the material and lead to detrimental side effects.[21,22] Additionally, in conventional water treatment systems, photocatalysts are typically dispersed in dye-containing aqueous solutions, where pollutants are degraded in the bulk phase following an initial adsorption–desorption equilibrium. While effective, these systems often suffer from complex separation procedures, poor catalyst recovery, materials instability, and the need to use metal-based photocatalytic materials. These limitations underscore the need for advanced remediation solutions that combine rapid pollutant capture with light-driven regeneration, while maintaining chemical and mechanical stability for long-term usage.

Herein, we introduce a multifunctional remediation strategy based on chemically inert, structurally robust photonic crystals that harness both architectural and optical advantages for the efficient removal of organic pollutants and their subsequent light-driven regeneration. Our design is built upon two synergistic principles. (1) The fabrication of highly ordered three-dimensional SiO_2 inverse opals (IOs) yields an interconnected porous scaffold that promotes rapid mass transport and effective adsorption of pollutant molecules. The chemical inertness of the silica framework ensures long-term structural and chemical integrity without risk of degradation, contaminant leaching, or surface chemistry modification. (2) The periodic modulation of refractive index within the inverse opal lattice generates slow photons and photonic bandgap effects. These unique optical phenomena enhance light trapping and promote the photoexcitation of embedded chromophoric organic pollutants, enabling direct, catalyst-free photodegradation within the photonic crystal framework. Our integrated design thus realizes a capture-and-photoregeneration mechanism that unites the benefits of adsorption and enhanced light-induced degradation while overcoming their respective limitations, even without the need for photocatalysts, elevated temperatures, or chemical additives.

In this study, we fabricate a series of SiO_2 inverse opal platforms with periodicities of 242 nm, 343 nm, and 400 nm to systematically tune their photonic bandgaps across the visible spectrum. All three inverse opal architectures exhibit rapid molecular adsorption, capturing over 80% pollutant within 15 minutes and exceeding 90% removal efficiency within 60 minutes under ambient, dark conditions. Upon subsequent visible light irradiation, the SiO_2 IO-343 platform shows the highest photodegradation performance, achieving 86% photobleaching of pre-adsorbed pollutants within one hour and reaching 95% with extended exposure to light. Notably, this design exhibits up to 17-fold and 2-fold higher apparent rate constant and photodegradation efficiency, respectively, compared to emerging decontamination platforms that rely on photonic-semiconductor or plasmonic-semiconductor hybrid photocatalysts. Mechanistic studies attribute the superior performance of SiO_2 IO-343 to enhanced light confinement *via* the slow photon effect and strong spectral overlap between the slow photon region and the pollutant's absorption band, both of which critically promote the photodegradation process. By uniting rapid pollutant adsorption with efficient photodegradation, this work establishes metal-free SiO_2 inverse opals as a robust and effective capture-and-photoregeneration platform for greener and sustainable water pollution treatment using light.

2. Results and discussion

To establish a multifunctional platform capable of both pollutant capture and photoregeneration, we prepare three-dimensional SiO_2 inverse opals (SiO_2 IOs) that combine periodic nanostructuring with chemical inertness. These inverse opal platforms leverage high surface area for molecular adsorption and photonic effects to enhance light–matter interactions (Fig. 1A). We begin by synthesizing monodisperse polystyrene (PS) nanoparticles with diameters of (302 ± 10) nm, (396 ± 20) nm, and (478 ± 15) nm *via* emulsion polymerization to serve as building blocks for the construction of opal-based sacrificial templates (Fig. S1).[23] Such size variations are important to precisely tune the resulting nanovoid diameters within the photonic crystals and control their photonic bandgap (PBG) positions across the visible spectrum. We then assemble the PS nanoparticles into highly ordered opal templates through sedimentation assisted by centrifugation (Fig. 1B and S2).[24] The resulting structures form a face-centered cubic (FCC) arrangement with over 100 particle layers, ensuring the quality required for high-fidelity inverse opal replication.

To construct the inverse opal lattices, we infiltrate the interstitial voids of the self-assembled PS opal templates with SiO_2 precursors using a vacuum-assisted process, followed by thermal calcination to remove the polymer scaffold (Fig. S3).[25] We confirm the successful formation of SiO_2 inverse opals with

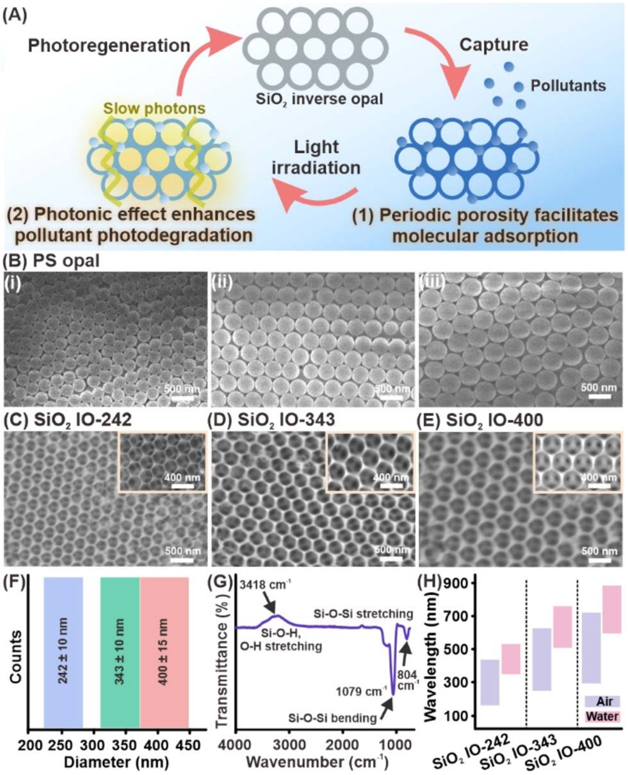

Fig. 1 (A) Schematic illustration of the multifunctional role of SiO_2 inverse opal photonic crystals in the rapid and efficient decontamination of chromogenic organic pollutants *via* a capture-and-photoregeneration mechanism. The highly porous structure facilitates pollutant adsorption, while the photonic architecture enhances light–matter interactions to drive effective self-photobleaching under visible light irradiation. (B) SEM images of opal-based photonic crystals fabricated using polystyrene (PS) nanoparticles with diameters of (i) 302 ± 10 nm, (ii) 396 ± 20 nm, and (iii) 478 ± 15 nm. SEM images of the corresponding SiO_2 inverse opals with pore sizes of (C) 242 ± 10 nm, (D) 343 ± 10 nm, and (E) 400 ± 15 nm. Insets show higher magnification SEM images highlighting the ordered porous architecture. (F) Pore size distribution of various SiO_2 inverse opals. (G) ATR-FTIR spectrum of SiO_2 IO-343. (H) Plot of photonic bandgap (PBG) positions calculated using Bragg's law for different SiO_2 IOs in both air and water environments across varying angles of incidence.

periodicities of (242 ± 10) nm, (343 ± 10) nm, and (400 ± 15) nm through SEM and structural characterization (Fig. 1C–F, S4 and S5). Based on their periodicities, we designate these structures as SiO_2 IO-242, SiO_2 IO-343, and SiO_2 IO-400. SEM imaging reveals well-preserved face-centered cubic (FCC)-like lattices with distinct sphere contact points, indicating high structural order even after template removal. All three structures exhibit 13–20% shrinkage in void size compared to the original opal templates. This shrinkage results from densification during calcination and is consistent with previous reports (Table S1).[26] The successful fabrication of these structurally tunable inverse opals is crucial to allow systematic investigation into how nanoscale architecture influences both adsorption kinetics and photonic enhancement of pollutant degradation under visible light.

We subsequently characterize the chemical and optical properties of the as-prepared SiO_2 inverse opal platforms to verify scaffold integrity and photonic behavior which are both essential for achieving efficient molecular adsorption and light-enhanced pollutant degradation. We first assess the chemical characteristics to confirm the formation of the silica scaffold, which provides chemical inertness critical for long-term structural and mechanical stability. ATR-FTIR analysis affirms the successful formation of silica frameworks across all inverse opal platforms, as evident from the distinct vibrational bands at 3418 cm^{-1} (O–H stretching of silanol groups and adsorbed water), 1079 cm^{-1}, and 804 cm^{-1} (Si–O–Si stretching) (Fig. 1G).[27] These vibrational signatures confirm the preservation of the silica network after thermal treatment, which is critical for ensuring chemical inertness and structural integrity. Additionally, the presence of surface silanol groups imparts hydrophilic character to the scaffold, a critical pre-requisite for facilitating strong interfacial interactions between the silica surfaces and aqueous-phase organic pollutants. Following chemical validation, we examine the optical properties to evaluate the photonic responses of various inverse opal structures (Fig. 1H and S6). Upon white light illumination, the SiO_2 inverse opals exhibit structural colors that are consistent with Bragg diffraction effects intrinsic to photonic crystals, whereby SiO_2 IO-242, SiO_2 IO-343, and SiO_2 IO-400 reflect blue, green-blue, and red light respectively (Fig. S7 and S8).[28] These colors align with their calculated PBG positions centered at approximately 480 nm, 600 nm, and 710 nm, respectively, and are further confirmed by diffuse reflectance spectroscopy (Fig. S9, S10, Table S2 and S3). We also observe a broadening of the PBGs, which likely originates from the three-dimensional architecture of the SiO_2 inverse opals that allows light to enter at a wide range of incident angles relative to the photonic crystal surfaces.[29] This periodic 3D scaffold enhances light–matter interactions that are important for visible-light-driven photodegradation of organic pollutants. Together, our findings validate the structural and functional integrity of the inverse opals, supporting their potential role as an effective decontamination platform.

In our design, the capture-and-photoregeneration strategy leverages (1) the rapid molecular adsorption enabled by the high surface area and interconnected porous architecture of the SiO_2 inverse opals, and (2) the light-trapping properties of the photonic crystal which enhance photodegradation efficiency through the generation of slow photons. To evaluate the adsorption performance, we select methylene blue (MB) as a model organic contaminant due to its high toxicity, widespread occurrence in wastewater from textile and pharmaceutical industries, and pronounced chromophoric properties in the visible regime.[17,18] We compare the adsorption capabilities of three different silica-based platforms that share identical material chemistry and nanoparticle size but differ in structural architecture (Fig. S11). These platforms include (1) SiO_2 IO-343 which features a highly porous and interconnected inverse opal network, (2) colloidal SiO_2 nanoparticles (325 nm) which represents a random particulate dispersion, and (3) SiO_2 opal-325 which has a compact periodic structure (Fig. S12). All platforms are immersed in a 5 ppm MB solution in the dark for

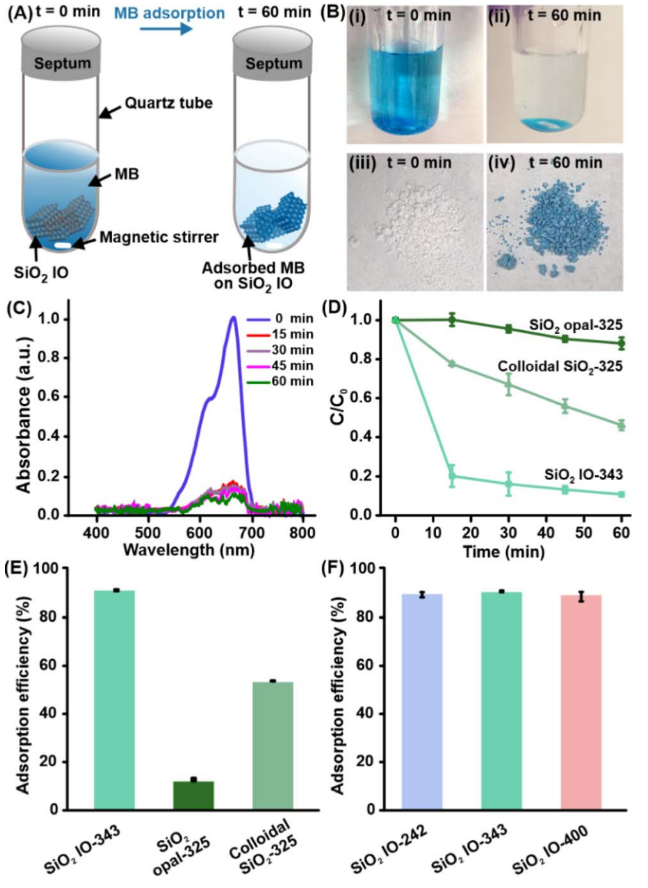

Fig. 2 (A) Schematic illustration of the adsorption process of methylene blue (MB) by SiO_2 inverse opals. (B) Digital images of SiO_2 IO-343 in (i, ii) aqueous MB solution and (iii, iv) powder form, before and after adsorption of MB from a 5 ppm solution, respectively. (C) UV-visible absorption spectra of MB solution after exposure to SiO_2 IO-343 under dark conditions for up to 60 min. (D) Time-dependent plots of normalized MB concentration (C/C_0) for different adsorbent platforms, comparing SiO_2 IO-343, colloidal SiO_2 (particle size, 325 nm), and SiO_2 opal-325. (E) Adsorption efficiency of MB for the three platforms shown in (D). (F) Comparison of MB adsorption efficiency among SiO_2 IOs with different pore sizes.

60 min to isolate the adsorption process and exclude any contributions from light-induced degradation (Fig. 2A). We extract aliquots of the sample solution at pre-defined time intervals over a 15 min period to quantify the remaining pollutant using its absorption peak at 667 nm and a standard calibration curve *via* UV-visible absorption spectroscopy (Fig. S13).

Notably, we observe that SiO_2 IO-343 rapidly decolorizes the aqueous MB solution and itself undergoes a distinct white-to-blue transition, indicating that methylene blue molecules are efficiently adsorbed onto the SiO_2 scaffold surfaces (Fig. 2B and C). Quantitative UV-visible absorption analysis further affirms that SiO_2 IO-343 removes over 85% of MB within the first 20 minutes and achieves ~90% removal after 60 minutes (Fig. 2D). When compared to the other two control platforms, SiO_2 IO-343 exhibits the highest adsorption capacity at 89%, followed by colloidal SiO_2 at 54%, and SiO_2 opal-325 at only 12% (Fig. 2E and S14). These differences in adsorption performance stem from the contrasting structural features of each platform. The inverse opal's open and interconnected porous architecture facilitates rapid mass transport and exposes a larger number of accessible adsorption sites. In contrast, the compact arrangement of solid spheres in SiO_2 opal limits surface exposure and restricts pore accessibility, thereby reducing its adsorption efficiency despite having the same periodicity as the inverse opal counterpart. Although colloidal SiO_2 particles are anticipated to offer more surface area than the SiO_2 opal, their lack of long-range order and continuous pore network constrains their ability to match the adsorption performance of the inverse opal.

Moreover, we further examine the influence of structural periodicity within the inverse opal architecture by comparing the MB adsorption performance of SiO_2 IO-242, SiO_2 IO-343, and SiO_2 IO-400 (Fig. 2F and S15). All platforms exhibit a similarly rapid transition from white to deep blue upon MB exposure, indicating consistent adsorption behavior across the series of inverse opal platforms. Time-dependent monitoring of the MB adsorption process shows that each inverse opal platform removes over 85% of MB within 60 min in the absence of light, signifying that equilibrium adsorption is reached within this period. The comparable adsorption efficiency across the three inverse opal platforms is attributed to the microporosity of their frameworks, which facilitates rapid diffusion of pollutant molecules and unrestricted access to internal adsorption sites. At the solid–liquid interface, MB adsorption is primarily driven by electrostatic interactions between cationic MB molecules and negatively charged silanol ($Si–O^-$) groups on the SiO_2 surface, with additional contributions from hydrogen bonding and van der Waals interactions. Despite differences in void size, the interconnected porous networks across all inverse opals provide ample surface area and mass transport channels, rendering the effect of periodicity on molecular adsorption is negligible. Collectively, our results affirm that while the inverse opal architecture is vital for efficient pollutant capture, variations in periodicity do not significantly influence adsorption kinetics in dilute conditions. To further evaluate the maximum adsorption capacity of various platforms, we conduct multiple adsorption cycles with periodic replacement of the dye solution (5 ppm) at 30 min intervals until saturation was achieved. Under these conditions, the differences in cumulative uptake become apparent, with SiO_2 IO-242 accommodating a larger total amount of MB (8.07 mg g_{silica}^{-1}) upon saturation in comparison to SiO_2 IO-343 (7.78 mg g_{silica}^{-1}) and SiO_2 IO-400 (5.56 mg g_{silica}^{-1}) (Fig. S16). This observation is attributed to its smaller void size, which provides a higher accessible internal surface area, while the interconnected porous network ensures efficient mass transport across all inverse opals. In contrast, the larger void sizes of SiO_2 IO-343 and SiO_2 IO-400 slightly reduce the available surface area per unit mass, resulting in lower cumulative adsorption capacities, although their interconnected porous networks still ensure efficient mass transport across all inverse opals. Overall, these results demonstrate that the inverse opals integrate a moderate adsorption capacity with efficient mass transport, supporting their suitability as photonic platforms with balanced adsorption functionality.

Having established the efficient adsorption of MB on SiO_2 inverse opals, we next assess their ability to mediate light-induced pollutant degradation and explore how structural periodicity modulates this performance. To isolate the effect of photodegradation, we gently rinse the MB-loaded scaffolds after 60 min of pollutant adsorption in dark and transfer them into fresh deionized water. This critical step removes residual dye from the solution, ensuring that subsequent decolorization originates solely from surface-adsorbed MB. To enable quantitative evaluation of pollutant removal, a colorimetric calibration curve is established by allowing the SiO_2 inverse opal to adsorb MB from aqueous solutions with concentrations ranging from 0 to 5 ppm (Fig. S17). Optical images of the platform are captured after equilibration at each concentration and RGB intensity values are extracted to generate the calibration curve of MB intensity index (Fig. 3A). This process enables subsequent image-based quantification of pollutant concentration during visible light irradiation. We then expose the pre-adsorbed platforms to white LED illumination ($\lambda > 400$ nm, 100 W) and capture images at 15 min intervals (Fig. 3B and S18). Colorimetric analysis of these snapshots yields an MB intensity index, where lower values indicate reduced amount of surface-bound dye and thus greater photodegradation efficiency. Control experiments confirm that MB remains chemically stable without light exposure and that the pre-adsorbed dye does not significantly redisperse into the surrounding aqueous solution during the course of the experiment (Fig. S19). These validations are essential to ensure that any observed color fading reflects true photodegradation at the photonic surfaces, rather than complications arising from dye desorption or its spontaneous decomposition under dark conditions.

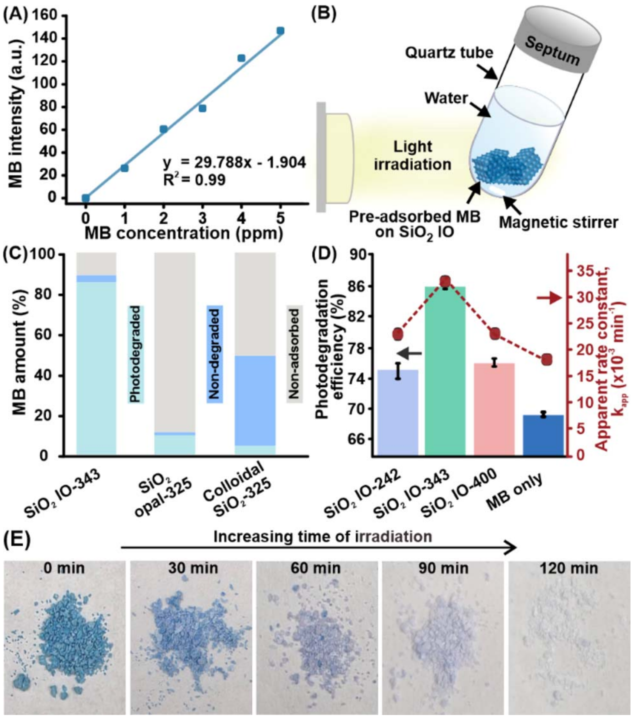

Fig. 3 (A) Calibration curve of MB absorbance intensity as a function of MB concentration. (B) Schematic of the experimental setup used to evaluate the photodegradation efficiency of pre-adsorbed MB on the SiO_2 inverse opal platforms under visible light irradiation. (C) Percentage of MB removal, accounting for adsorption, photodegradation, and residual (non-degraded) content across different platforms. (D) Comparison of photodegradation efficiency and apparent rate constants (k_{app}) representing the MB's photobleaching kinetics across different inverse opal platforms and MB-only control after 1 h of light exposure. (E) Time-resolved digital images showing the progressive photodegradation of pre-adsorbed MB on SiO_2 IO-343 across 2 h of irradiation.

Among all tested platforms, SiO_2 IO-343 exhibits the most pronounced decolorization of the pre-adsorbed organic pollutant upon light irradiation (Fig. S20). Its initially intense blue appearance (MB intensity ~130 a.u.) fades markedly under light exposure, reaching 16.6 a.u. after 60 minutes which corresponds to a photodegradation efficiency of 86% (Fig. S21). When benchmarked against structurally distinct yet chemically identical control platforms, the SiO_2 IO-343 achieves higher photodegradation performance to SiO_2 opal (9.6%) or far superior performance relative to colloidal SiO_2 nanoparticles (4.4%; Fig. 3C). We note that although the colloidal SiO_2 platform demonstrates higher initial adsorption, its disordered structure lacks the ability to confine and manipulate light, resulting in minimal photodegradation. In contrast, the SiO_2 opal, albeit its lower adsorption capacity, facilitates notable dye degradation which can be attributed to the photonic enhancement afforded by its periodic structure (Fig. S22 and Table S4). It is also worth mentioning that our best-performing SiO_2 IO-343 maintains high decontamination efficiency even in a more complex pollutant environment containing volatile organic solvents (*e.g.*, 10% ethanol), achieving over 90% pollutant capture and photodegradation efficiency (Fig. S23 and S24). This consistent performance indicates that the platform's adsorption sites remain accessible and functional, and that its photonic architecture continues to confine light effectively even in more complex pollutant environments. The results highlight the importance of photonic crystal structures in amplifying light–matter interactions and driving effective, catalyst-free pollutant breakdown under visible light illumination.

More importantly, we examine the impact of photonic band alignment by comparing the photodegradation performance of SiO_2 inverse opals with different void sizes (Fig. 3D). SiO_2 IO-343 consistently exhibits superior photodegradation efficiency, achieving 86% degradation after 60 min of light exposure. In contrast, SiO_2 IO-242 and SiO_2 IO-400 achieve lower efficiencies of 75% and 76%, respectively, which are only marginally higher than the 69% efficiency observed in the MB-only control without any photonic platform. Kinetic analysis using the integrated first-order rate law, $-\ln(C/C_0) = k_{app}\,t$, reveals that SiO_2 IO-343 exhibits the highest apparent rate constant ($k_{app} = 0.033\ min^{-1}$), surpassing both SiO_2 IO-242 and SiO_2 IO-400 by up to 1.4-fold and exceeding the intrinsic MB photobleaching by 1.7-fold (Fig. S25). Extending the irradiation period to a 120 min duration further enhances SiO_2 IO-343's performance, reaching a photodegradation efficiency of 95% (MB intensity: 4.59 a.u.) which represents a 1.4-fold improvement over intrinsic MB photolysis (Fig. 3E, S26 and S27).

Systematic comparisons of the optical profiles of the photonic crystals and MB's absorption spectrum attribute SiO_2 IO-343's enhanced photodegradation capability to the strongest spectral overlap between its PBG and MB's absorption band (Fig. 4A). In contrast, SiO_2 IO-242 and SiO_2 IO-400 possess PBGs that are misaligned with MB's absorption region, thereby demonstrating relatively weaker improvements in photodegradation kinetics of ~1.2-fold (Table S3). Our findings clearly demonstrate that although internal light scattering contributes to some enhancement across all inverse opals, only platforms with well-aligned photonic features with the organic pollutant's chromophore can fully exploit slow photon effects to drive its efficient photodegradation.

To further elucidate the mechanism behind the enhanced light-induced pollutant degradation observed in SiO_2 IO-343, we systematically investigate its photoreactivity under monochromatic light sources (Fig. 4B). Incident wavelengths of 600 nm, 650 nm, and 700 nm are chosen to assess how the alignment between PBG edges and excitation wavelengths influences slow photon generation (Fig. S28 and S29). The 650 nm light closely aligns with both the red edge of the PBG in SiO_2 IO-343 and the absorption maximum of MB at 667 nm, making it ideal for evaluating the impact of spectral overlap on photodegradation activity. In contrast, 600 nm and 700 nm serve as reference points outside this alignment range. We observe that 650 nm illumination results in the most efficient photobleaching among the monochromatic sources, confirming that slow photons are effectively generated when the incident light matches the PBG edge (Fig. S30). These slow photons enhance the excitation of MB molecules, increasing the likelihood of their photochemical decomposition. Interestingly, white light irradiation yields even higher photodegradation performance, outperforming 600 nm, 650 nm, and 700 nm by 1.4-fold, 1.2-fold, and 1.7-fold, respectively. This superior performance is attributed to the broadband nature of white light which spans a wider range of wavelengths and thus overlaps more extensively with the PBG, enabling the simultaneous generation of slow photons across the visible spectrum. Moreover, the three-dimensional geometry of the inverse opal plays a pivotal role by enabling omnidirectional light trapping, which maximizes photon–pollutant interactions across a broad range of incident angles and further amplifies the photonic enhancement effect. These optical advantages work in concert with the highly porous, interconnected architecture, and hydrophilic surface chemistry (*e.g.*, silanol group) of the SiO_2 scaffold, collectively providing abundant and accessible adsorption sites while promoting strong interfacial interactions with aqueous-phase pollutants.[30,31] Following molecular adsorption under dark conditions, MB molecules confined within the inverse opal framework experience enhanced photoexcitation during light irradiation when the slow photon wavelengths overlap with the dye's absorption band. This enhanced light confinement increases the excitation probability of surface-bound MB molecules, promoting electronic transitions to excited singlet and triplet states. These excited states subsequently undergo photooxidative pathways, including interactions with dissolved oxygen,[32,33] leading to chromophore break down (*i.e.*, conversion of MB into its colorless leuco form) and photobleaching. Importantly, the absence of semiconductors or redox-active species indicates that degradation proceeds *via* direct photoexcitation of the dye, amplified by the photonic crystal environment. This synergistic integration of high adsorption capacity and slow photon-enhanced photoexcitation thus establishes an effective capture-and-photoregeneration pathway, enabling SiO_2 IO-343 to achieve rapid and effective decontamination of organic pollutants using visible light as a green and widely accessible energy source (Fig. 4C).

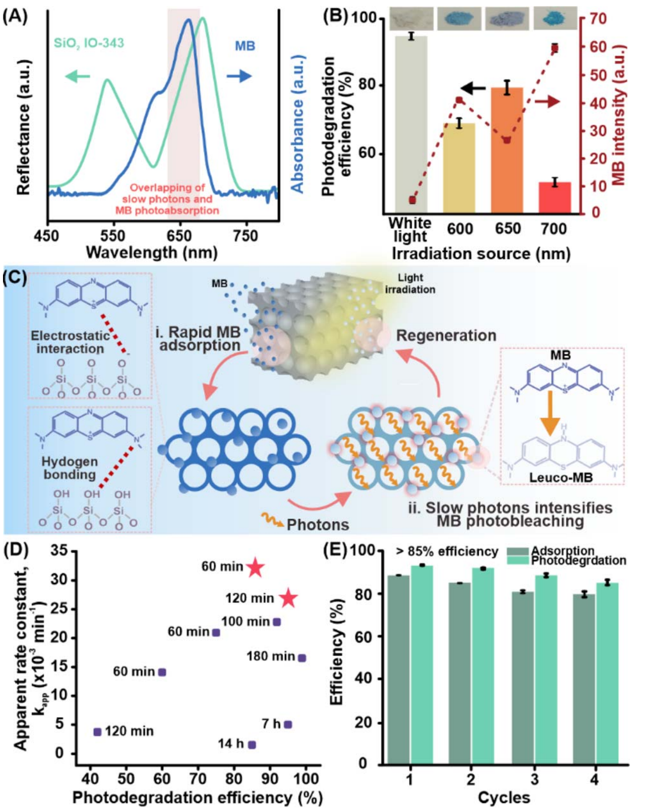

Fig. 4 (A) Reflectance spectrum of SiO_2 IO-343 and absorption spectrum of MB. (B) Photodegradation efficiency and corresponding MB intensity by SiO_2 IO-343 upon irradiation with white light and various monochromatic lights for 2 h. (C) Proposed mechanism illustrating rapid adsorption-based decontamination of aqueous MB and subsequent photoregeneration, enhanced by light harvesting and the slow photon effect in the photonic structure. (D) Comparison of photodegradation rate constants for chromogenic organic pollutant removal using the SiO_2 IO-343 platform in this work with selected literature reports involving photonic crystals and hybrid plasmonic-semiconductor photocatalysts under light irradiation. (E) Recyclability performance of SiO_2 IO-343 over four consecutive capture-and-photoregeneration cycles. Each cycle consists of 1 h of pollutant adsorption in dark conditions followed by 2 h of visible light irradiation.

Our findings collectively highlight the potential of photonic crystal architectures in enabling efficient, light-driven decontamination without relying on traditional catalysts or optically active materials. Notably, the SiO_2 IO-343 platform achieves high apparent rate constant up to 17-fold greater than those reported for state-of-the-art hybrid photocatalytic systems comprising semiconductors, plasmonic nanostructures, or composite photonic–plasmonic ensembles (Fig. 4D and Table S5). Unlike these conventional approaches, our platform is entirely catalyst-free and constructed solely from optically and chemically inert silica building blocks, yet it still delivers superior performance by effectively combining broadband light harvesting, slow photon enhancement, and high surface accessibility enabled by the inverse opal architecture. Beyond its performance, the SiO_2 IO-343 also maintains its structural and chemical integrity over prolonged usage. Reusability tests affirm the platform retains its photonic features and pollutant decontamination efficiency across four cycles, with <10% deviation in adsorption and photodegradation performances even without requiring intermediate chemical treatments (Fig. 4E and S31). This observation also extends to other inverse opal variants such as SiO_2 IO-242 and SiO_2 IO-400, underscoring the general mechanical and chemical stability of the SiO_2 inverse opal design. (Fig. S32 and S33). To evaluate the generality of the SiO_2 IO toward other organic molecules beyond MB, we further expand our test scope to malachite green (MG) and rhodamine 6G (R6G) as representative commercial dyes and employed SiO_2 IO-343 as the model platform (Supporting text 1 and 2, Fig. S34–S48). Kinetic analysis reveals that SiO_2 IO-343 enhances the photodegradation rate of MG by approximately 10-fold compared to intrinsic photobleaching. In the case of R6G, SiO_2IO-343 achieves a photodegradation efficiency of 46% (with the R6G intensity fading from ∼40 a.u. to ∼21 a.u.) and exhibits an approximately 1.7-fold enhancement in photodegradation kinetics relative to intrinsic photobleaching. Overall, these results clearly demonstrate that the SiO_2 inverse opal platform can effectively adsorb and photodegrade a wide range of structurally distinct organic pollutants by leveraging wavelength-selective slow photon enhancement, thereby highlighting its versatility and tunability for broader photocatalytic applications (Fig. S49).

3. Conclusion

In conclusion, we have demonstrated an efficient strategy for organic pollutant photodegradation using our multifunctional SiO_2 inverse opal platforms. These structures leverage a synergistic capture-and-photoregeneration mechanism, whereby (1) chromophoric pollutants are rapidly adsorbed onto the porous, periodic silica framework, (2) the pre-adsorbed molecules undergo enhanced photodegradation under visible light exposure, and (3) the platform regenerates without requiring external chemical treatment. Among the tested designs, SiO_2 IO-343 exhibits superior performance, achieving >89% adsorption within 60 minutes under dark conditions and up to 95% photodegradation upon extended irradiation, with an apparent rate constant of >0.027 min^{-1}. This high activity is attributed to the optimal spectral alignment between the photonic bandgap of the SiO_2 IO architecture and the absorption band of the chromophoric organic pollutant. This alignment facilitates slow photon generation at the PBG edges, enhancing local light confinement and enabling efficient excitation of the pollutant's chromophores, which in turn accelerates photobleaching reactions. The three-dimensional periodicity further contributes to omnidirectional light trapping, maximizing the interaction between photons and target molecules across a broad range of incident angles. The platform also maintains consistent decontamination performance over four consecutive cycles (>85% efficiency retention) without any intermediate regeneration steps, underscoring its structural integrity and operational durability. More importantly, this catalyst-free and chemically inert system achieves photodegradation performance that rivals or surpasses that of many hybrid photocatalytic systems by up to 17-fold, all without relying on semiconductors, redox-active dopants, or sacrificial agents. Altogether, these findings position inverse opal photonic architectures as a synergistic platform that unites the rapid capture capacity of adsorbents with the degradative power of reaction-based treatments, while overcoming their individual drawbacks such as finite capacity, secondary waste generation, and inherent instability. Beyond serving as stand-alone decontamination platforms, the underlying design principles can be extended to integrate with semiconductor photocatalysts or other photoactive materials, paving the way for next-generation, versatile, and multifunctional light-driven platforms for efficient water purification applications and beyond.

4. Experimental procedures

For experimental details, see the supplementary information (SI).

Conflicts of interest

There are no conflicts to declare.

Data availability

The data supports the findings of this study are available from the corresponding author upon request.

Supplementary information (SI) is available. See DOI: https://doi.org/10.1039/d5ta09484d.

Acknowledgements

H.K.L. thanks the funding supports from the Singapore Ministry of Education (AcRF Tier 1 RG92/24), Agency for Science, Technology and Research (A*STAR, Singapore; MTC IRG M23M6c0098), and the Nanyang Technological University start-up grants.

References

1 S. B. Grant, J.-D. Saphores, D. L. Feldman, A. J. Hamilton, T. D. Fletcher, P. L. M. Cook, M. Stewardson, B. F. Sanders, L. A. Levin, R. F. Ambrose, A. Deletic, R. Brown, S. C. Jiang, D. Rosso, W. J. Cooper and I. Marusic, *Science*, 2012, **337**, 681–686.

2 C. J. Vorosmarty, P. B. McIntyre, M. O. Gessner, D. Dudgeon, A. Prusevich, P. Green, S. Glidden, S. E. Bunn, C. A. Sullivan, C. R. Liermann and P. M. Davies, *Nature*, 2010, **467**, 555–561.
3 K. Bakker, *Science*, 2012, **337**, 914–915.
4 S. Dutta, S. Adhikary, S. Bhattacharya, D. Roy, S. Chatterjee, A. Chakraborty, D. Banerjee, A. Ganguly, S. Nanda and P. Rajak, *J. Environ. Manag.*, 2024, **353**, 120103.
5 J. Lin, W. Ye, M. Xie, D. H. Seo, J. Luo, Y. Wan and B. Van der Bruggen, *Nat. Rev. Earth Environ.*, 2023, **4**, 785–803.
6 N. Gonzalez, M. V. Aguinaga Martínez, C. E. Domini and C. C. Acebal, *Trends Environ. Anal. Chem.*, 2023, **37**, e00197.
7 M. Muz, J. P. Dann, F. Jager, W. Brack and M. Krauss, *Environ. Sci. Technol.*, 2017, **51**, 4681–4688.
8 B. S. Rathi and P. S. Kumar, *Environ. Pollut.*, 2021, **280**, 116995.
9 S. Krishnamoorthy, F. Ajala, S. M. Mohammed, A. Asok and S. Shukla, *Appl. Surf. Sci.*, 2021, **548**, 149265.
10 S. Rojas and P. Horcajada, *Chem. Rev.*, 2020, **120**, 8378–8415.
11 Y. Song, J. Phipps, C. Zhu and S. Ma, *Angew. Chem., Int. Ed.*, 2023, **62**, e202216724.
12 P. Sherugar, M. Padaki, N. S. Naik, S. D. George and D. H. K. Murthy, *Chemosphere*, 2022, **287**, 132085.
13 N. A. A. Qasem, R. H. Mohammed and D. U. Lawal, *npj Clean Water*, 2021, **4**, 36.
14 W. Wang, Y. Zhao, H. Bai, T. Zhang, V. Ibarra-Galván and S. Song, *Carbohydr. Polym.*, 2018, **198**, 518–528.
15 T. Zhang, W. Wang, Y. Zhao, H. Bai, T. Wen, S. Kang, G. Song, S. Song and S. Komarneni, *Chem. Eng. J.*, 2021, **420**, 127574.
16 S. C. R. Marques, J. M. Marcuzzo, M. R. Baldan, A. S. Mestre and A. P. Carvalho, *Chem. Eng. J.*, 2017, **321**, 233–244.
17 W. Li, C. Cheng, J. Zhao, Y. Song and C. Xue, *Angew. Chem., Int. Ed.*, 2025, **64**, e202425508.
18 F. Wang, F.-L. Li, M.-M. Xu, H. Yu, J.-G. Zhang, H.-T. Xia and J.-P. Lang, *J. Mater. Chem. A*, 2015, **3**, 5908–5916.
19 C.-C. Wang, J.-R. Li, X.-L. Lv, Y.-Q. Zhang and G. Guo, *Energy Environ. Sci.*, 2014, **7**, 2831–2867.
20 X. Yang, H. Sun, G. Li, T. An and W. Choi, *Appl. Catal., B*, 2021, **294**, 120252.
21 S. Kumar, V. Sharma, K. Bhattacharyya and V. Krishnan, *Mater. Chem. Front.*, 2017, **1**, 1093–1106.
22 J. Zhang, A. Bifulco, P. Amato, C. Imparato and K. Qi, *J. Colloid Interface Sci.*, 2023, **638**, 193–219.
23 J.-F. Fang, Y.-M. Xuan and Q. Li, *Sci. China Technol. Sci.*, 2010, **53**, 3088–3093.
24 Q. Zhou, P. Dong, L. Liu and B. Cheng, *Colloids Surf., A*, 2005, **253**, 169–174.
25 Y. Zhang, K. Li, F. Su, Z. Cai, J. Liu, X. Wu, H. He, Z. Yin, L. Wang, B. Wang, Y. Tian, D. Luo, X. W. Sun and Y. J. Liu, *Opt. Express*, 2019, **27**, 15391–15398.
26 M. Curti, G. López Robledo, P. C. dos Santos Claro, J. H. Ubogui and C. B. Mendive, *Mater. Res. Bull.*, 2018, **101**, 12–19.
27 L. Tillman, A. Voskanyan and A. Navrotsky, *J. Am. Ceram. Soc.*, 2023, **106**, 1993–1999.
28 G. L. Chiarello, A. Zuliani, D. Ceresoli, R. Martinazzo and E. Selli, *ACS Catal.*, 2016, **6**, 1345–1353.
29 R. K. Cersonsky, J. Antonaglia, B. D. Dice and S. C. Glotzer, *Nat. Commun.*, 2021, **12**, 2543.
30 J. Antony, S. Villa Gonzalez, S. Bandyopadhyay, J. Yang and M. Rønning, *Catal. Today*, 2023, **413–415**, 113986.
31 R. Lyu, C. Zhang, T. Xia, S. Chen, Z. Wang, X. Luo, L. Wang, Y. Wang, J. Yue and C. Wang, *Colloids Surf., A*, 2020, **606**, 125425.
32 Z. Kalaycioglu, B. O. Uysal, O. Pekcan and F. B. Erim, *ACS Omega*, 2023, **8**, 13004–13015.
33 D. Atta, H. A. Wahab, M. A. Ibrahim and I. K. Battisha, *Sci. Rep.*, 2024, **14**, 26961.